
COT-GAN: GENERATING SEQUENTIAL DATA VIA CAUSAL OPTIMAL TRANSPORT

A PREPRINT

Tianlin Xu
London School of Economics

Li K. Wenliang
University College London

Michael Munn
Google

Beatrice Acciaio*
London School of Economics

ABSTRACT

We introduce COT-GAN, an adversarial algorithm to train implicit generative models optimized for producing sequential data. The loss function of this algorithm is formulated using ideas from Causal Optimal Transport (COT), which combines classic optimal transport methods with an additional temporal causality constraint. Remarkably, we find that this causality condition provides a natural framework to parameterize the cost function that is learned by the discriminator as a robust (worst-case) distance, and an ideal mechanism for learning time dependent data distributions. Following Genevay et al. (2018), we also include an entropic penalization term which allows for the use of the Sinkhorn algorithm when computing the optimal transport cost. Our experiments show effectiveness and stability of COT-GAN when generating both low- and high-dimensional time series data. The success of the algorithm also relies on a new, improved version of the Sinkhorn divergence which demonstrates less bias in learning.

1 Introduction

Dynamical data are ubiquitous in the world, including natural scenes such as video and audio data, and temporal recordings such as physiological and financial traces. Being able to synthesize realistic dynamical data is a challenging unsupervised learning problem and has wide scientific and practical applications. In recent years, training implicit generative models (IGMs) has proven to be a promising approach to data synthesis, driven by the work on generative adversarial networks (GANs) [22].

Nonetheless, training IGMs on dynamical data poses an interesting yet difficult challenge. On one hand, learning complex dependencies between spatial locations and channels for static images has already received significant effort within the research community. On the other hand, temporal dependencies are no less complicated since the dynamical features are strongly correlated with spatial features. Recent works, including [34, 42, 15, 39, 36], often tackle this problem by separating the model or loss into static and dynamic components.

In this paper, we consider training dynamic IGMs for sequential data. We introduce a **new adversarial objective** that builds on optimal transport (OT) theory, and constrains the transport plans to respect *causality*: the probability mass moved to the target sequence at time t can only depend on the source sequence up to time t [3, 7]. A reformulation of the causality constraint leads to a formulation of an adversarial training objective in the spirit of [19], but tailored to sequential data. In addition, we demonstrate that optimizing the original Sinkhorn divergence over mini-batches causes biased parameter estimation, and propose the **mixed Sinkhorn divergence** which avoids this problem. Our new framework, Causal Optimal Transport GAN (COT-GAN), outperforms existing methods on a wide range of datasets from traditional time series to high dimensional videos.

*We would like to thank the financial support from the Erwin Schrödinger Institute during the thematic programme on Optimal Transport (May 2019, Vienna)

2 Background

2.1 Adversarial learning for implicit generative models

Goodfellow et al. [22] introduced an adversarial scheme for training an IGM. Given a (real) data distribution $\mu = \frac{1}{N} \sum_{i=1}^N \delta_{x^i}$, $x^i \in \mathcal{X}$, and a distribution ζ on some latent space \mathcal{Z} , the generator is a function $g : \mathcal{Z} \rightarrow \mathcal{X}$ trained so that the induced distribution $\nu = \zeta \circ g^{-1}$ is as close as possible to μ as judged by a discriminator. The discriminator is a function $f : \mathcal{X} \rightarrow [0, 1]$ trained to output a high value if the input is real (from μ), and a low value otherwise (from ν). In practice, the two functions are implemented as neural networks g_θ and f_φ with parameters θ and φ , and the generator distribution is denoted by ν_θ . The training objective is then formulated as a zero-sum game between the generator and the discriminator. Different probability divergences were later proposed to evaluate the distance between μ and ν_θ [30, 26, 29, 4]. Notably, the Wasserstein-1 distance was used in [6, 5]:

$$\mathcal{W}_1(\mu, \nu) = \inf_{\pi \in \Pi(\mu, \nu)} \mathbb{E}^\pi[\|x - y\|_1], \quad (2.1)$$

where $\Pi(\mu, \nu)$ is the space of transport plans (couplings) between μ and ν . Its dual form turns out to be a maximization problem over φ such that f_φ is Lipschitz. Combined with the minimization over θ , a min-max problem can be formulated with a Lipschitz constraint on f_φ .

2.2 Optimal transport and Sinkhorn divergences

The optimization in (2.1) is a special case of the classical (Kantorovich) optimal transport problem. Given probability measures μ on \mathcal{X} , ν on \mathcal{Y} , and a cost function $c : \mathcal{X} \times \mathcal{Y} \rightarrow \mathbb{R}$, the optimal transport problem is formulated as

$$\mathcal{W}_c(\mu, \nu) := \inf_{\pi \in \Pi(\mu, \nu)} \mathbb{E}^\pi[c(x, y)]. \quad (2.2)$$

Here, $c(x, y)$ represents the cost of transporting a unit of mass from $x \in \mathcal{X}$ to $y \in \mathcal{Y}$, and $\mathcal{W}_c(\mu, \nu)$ is thus the minimal total cost to transport the mass from μ to ν . Obviously, the Wasserstein-1 distance (2.1) corresponds to $c(x, y) = \|x - y\|_1$. However, when μ and ν are supported on finite sets of size n , solving (2.2) has super-cubic (in n) complexity [14, 31, 32], which is computationally expensive for large datasets.

Instead, Genevay et al. [19] proposed training IGMs by minimizing a regularized Wasserstein distance that can be computed more efficiently by the Sinkhorn algorithm (see [14]). For transport plans with marginals μ supported on a finite set $\{x^i\}_i$ and ν on a finite set $\{y^j\}_j$, any $\pi \in \Pi(\mu, \nu)$ is also discrete with support on the set of all possible pairs $\{(x^i, y^j)\}_{i,j}$. Denoting $\pi_{ij} = \pi(x^i, y^j)$, the Shannon entropy of π is given by $H(\pi) := -\sum_{i,j} \pi_{ij} \log(\pi_{ij})$. For $\varepsilon > 0$, the regularized optimal transport problem then reads as

$$\mathcal{P}_{c,\varepsilon}(\mu, \nu) := \inf_{\pi \in \Pi(\mu, \nu)} \{\mathbb{E}^\pi[c(x, y)] - \varepsilon H(\pi)\}. \quad (2.3)$$

Denoting by $\pi_{c,\varepsilon}(\mu, \nu)$ the optimizer in (2.3), one can define a regularized distance by

$$\mathcal{W}_{c,\varepsilon}(\mu, \nu) := \mathbb{E}^{\pi_{c,\varepsilon}(\mu, \nu)}[c(x, y)]. \quad (2.4)$$

Computing this distance is numerically more stable than solving the dual formulation of the OT problem, as the latter requires differentiating dual Kantorovich potentials; see e.g. [12, Proposition 3]. To correct the fact that $\mathcal{W}_{c,\varepsilon}(\alpha, \alpha) \neq 0$, Genevay et al. [19] proposed to use the *Sinkhorn divergence*:

$$\widehat{\mathcal{W}}_{c,\varepsilon}(\mu, \nu) := 2\mathcal{W}_{c,\varepsilon}(\mu, \nu) - \mathcal{W}_{c,\varepsilon}(\mu, \mu) - \mathcal{W}_{c,\varepsilon}(\nu, \nu) \quad (2.5)$$

as the objective function, and to learn the cost $c_\varphi(x, y) = \|f_\varphi(x) - f_\varphi(y)\|$ parameterized by φ , resulting in the following adversarial objective

$$\inf_{\theta} \sup_{\varphi} \widehat{\mathcal{W}}_{c_\varphi, \varepsilon}(\mu, \nu_\theta), \quad (2.6)$$

In practice, a sample-version of this cost is used, where μ and ν are replaced by distributions of mini-batches randomly extracted from them.

3 Training generative models with Causal Optimal Transport

We now focus on data that consists of d -dimensional (number of channels), T -long sequences, so that μ and ν are distributions on the path space $\mathbb{R}^{d \times T}$. In this setting we introduce a special class of transport plans, between $\mathcal{X} = \mathbb{R}^{d \times T}$ and $\mathcal{Y} = \mathbb{R}^{d \times T}$, that will be used to define our objective function. On $\mathcal{X} \times \mathcal{Y}$, we denote by $x = (x_1, \dots, x_T)$ and $y = (y_1, \dots, y_T)$ the first and second half of the coordinates, and we let $\mathcal{F}^{\mathcal{X}} = (\mathcal{F}_t^{\mathcal{X}})_{t=1}^T$ and $\mathcal{F}^{\mathcal{Y}} = (\mathcal{F}_t^{\mathcal{Y}})_{t=1}^T$ be the canonical filtrations (for all t , $\mathcal{F}_t^{\mathcal{X}}$ is the smallest σ -algebra s.t. $(x_1, \dots, x_T) \mapsto (x_1, \dots, x_t)$ is measurable; analogously for $\mathcal{F}^{\mathcal{Y}}$).

3.1 Causal Optimal Transport

Definition 3.1. A transport plan $\pi \in \Pi(\mu, \nu)$ is called causal if

$$\pi(dy_t | dx_1, \dots, dx_T) = \pi(dy_t | dx_1, \dots, dx_t) \quad \text{for all } t = 1, \dots, T-1.$$

The set of all such plans will be denoted by $\Pi^{\mathcal{K}}(\mu, \nu)$.

Roughly speaking, the amount of mass transported by π to a subset of the target space \mathcal{Y} belonging to $\mathcal{F}_t^{\mathcal{Y}}$ depends on the source space \mathcal{X} only up to time t . Thus, a causal plan transports μ into ν in a non-anticipative way, which is a natural request in a sequential framework. In the present paper, we will use causality in the sense of Definition 3.1. However, note that in the literature, the term causality is often used to indicate a mapping in which the output at a given time t depends only on inputs up to time t .

Restricting the space of transport plans to $\Pi^{\mathcal{K}}$ in the OT problem (2.2) gives the COT problem

$$\mathcal{K}_c(\mu, \nu) := \inf_{\pi \in \Pi^{\mathcal{K}}(\mu, \nu)} \mathbb{E}^{\pi}[c(x, y)]. \quad (3.1)$$

COT has already found wide application in dynamic problems in stochastic calculus and mathematical finance, see e.g. [2, 1, 3, 9, 8]. The causality constraint can be equivalently formulated in several ways, see [7, Proposition 2.3]. The one that will be useful for our purposes can be expressed in the following way: let $\mathcal{M}(\mathcal{F}^{\mathcal{X}}, \mu)$ be the set of $(\mathcal{X}, \mathcal{F}^{\mathcal{X}}, \mu)$ -martingales, and define

$$\mathcal{H}(\mu) := \{(h, M) : h = (h_t)_{t=1}^{T-1}, h_t \in \mathcal{C}_b(\mathbb{R}^t), M = (M_t)_{t=1}^T \in \mathcal{M}(\mathcal{F}^{\mathcal{X}}, \mu), M_t \in \mathcal{C}_b(\mathbb{R}^t)\},$$

then a transport plan $\pi \in \Pi(\mu, \nu)$ is causal if and only if

$$\mathbb{E}^{\pi} \left[\sum_{t=1}^{T-1} h_t(y_{\leq t}) \Delta_{t+1} M(x_{\leq t+1}) \right] = 0 \quad \text{for all } (h, M) \in \mathcal{H}(\mu), \quad (3.2)$$

where $x_{\leq t} := (x_1, x_2, \dots, x_t)$ and similarly for $y_{\leq t}$, and $\Delta_{t+1} M(x_{\leq t+1}) := M_{t+1}(x_{\leq t+1}) - M_t(x_{\leq t})$. As usual, $\mathcal{C}_b(\mathbb{X})$ denotes the space of continuous, bounded functions on \mathbb{X} . Where no confusion can arise, with an abuse of notation we will simply write $h_t(y), M_t(x), \Delta_{t+1} M(x)$ rather than $h_t(y_{\leq t}), M_t(x_{\leq t}), \Delta_{t+1} M(x_{\leq t+1})$.

3.2 Regularized Causal Optimal Transport

In the same spirit of [19], we include an entropic regularization in the COT problem (3.1) and consider

$$\mathcal{P}_{c,\varepsilon}^{\mathcal{K}}(\mu, \nu) := \inf_{\pi \in \Pi^{\mathcal{K}}(\mu, \nu)} \{\mathbb{E}^{\pi}[c(x, y)] - \varepsilon H(\pi)\}. \quad (3.3)$$

The solution to such problem is then unique due to strict concavity of H . We denote by $\pi_{c,\varepsilon}^{\mathcal{K}}(\mu, \nu)$ the optimizer to the above problem, and define the regularized COT distance by

$$\mathcal{K}_{c,\varepsilon}(\mu, \nu) := \mathbb{E}^{\pi_{c,\varepsilon}^{\mathcal{K}}(\mu, \nu)}[c(x, y)].$$

Remark 3.2. In analogy to the non-causal case, it can be shown that, for discrete μ and ν (as in practice), the following limits holds:

$$\mathcal{K}_c(\mu, \nu) \xleftarrow[\varepsilon \rightarrow 0]{} \mathcal{K}_{c,\varepsilon}(\mu, \nu) \xrightarrow[\varepsilon \rightarrow \infty]{} \mathbb{E}^{\mu \otimes \nu}[c(x, y)],$$

where $\mu \otimes \nu$ denotes the independent coupling.

See Appendix A.1 for a proof. This means that the regularized COT distance is between the COT distance and the loss obtained by independent coupling, and is closer to the former for small ε . Optimizing over the space of causal plans $\Pi^{\mathcal{K}}(\mu, \nu)$ is not straightforward. Nonetheless, the following proposition shows that the problem can be reformulated as a maximization over non-causal problems with respect to a specific family of cost functions.

Proposition 3.3. The regularized COT problem (3.3) can be reformulated as

$$\mathcal{P}_{c,\varepsilon}^{\mathcal{K}}(\mu, \nu) = \sup_{l \in \mathcal{L}(\mu)} \mathcal{P}_{c+l, \varepsilon}(\mu, \nu), \quad (3.4)$$

where

$$\mathcal{L}(\mu) := \left\{ \sum_{j=1}^J \sum_{t=1}^{T-1} h_t^j(y) \Delta_{t+1} M^j(x) : J \in \mathbb{N}, (h^j, M^j) \in \mathcal{H}(\mu) \right\}. \quad (3.5)$$

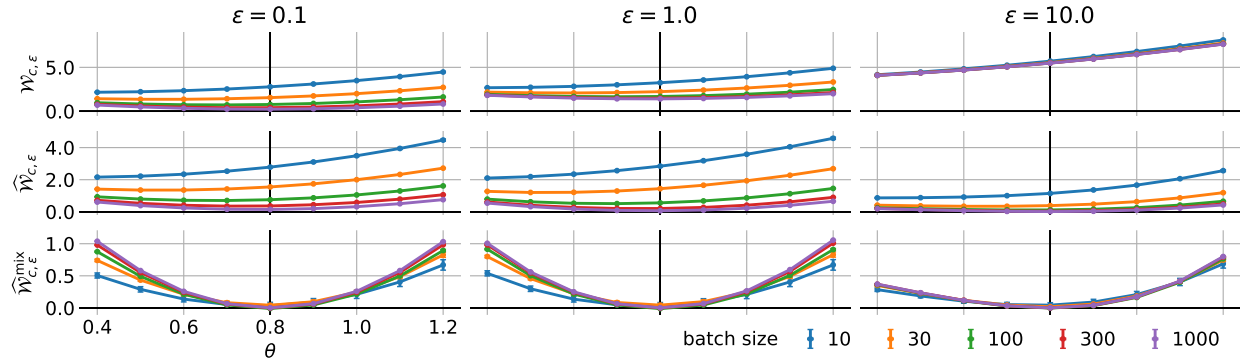


Figure 1: Regularized distance (2.4), Sinkhorn divergence (2.5) and mixed Sinkhorn divergence (3.8) computed for mini-batches of size m from μ and ν_θ , where $\mu = \nu_{0.8}$. Color indicates batch size. Curve and errorbar show the mean and sem estimated from 300 draws of mini-batches.

This means that the optimal value of the regularized COT problem equals the maximum value over the family of regularized OT problems w.r.t. the set of cost functions $\{c + l : l \in \mathcal{L}(\mu)\}$. This result has been proven in [3]. As it is crucial for our analysis, we show it in Appendix A.2.

Proposition 3.3 suggests the following worst-case distance between μ and ν :

$$\sup_{l \in \mathcal{L}(\mu)} \mathcal{W}_{c+l, \varepsilon}(\mu, \nu), \quad (3.6)$$

as a regularized Sinkhorn distance that respects the causal constraint on the transport plans.

In the context of training a dynamic IGM, the training dataset is a collection of paths $\{x^i\}_{i=1}^N$ of equal length T , $x^i = (x_1^i, \dots, x_T^i)$, $x_T^i \in \mathbb{R}^d$. As N is usually very large, we proceed as usual by approximating $\mathcal{W}_{c+l, \varepsilon}(\mu, \nu)$ with its empirical mini-batch counterpart. Precisely, for a given IGM g_θ , we fix a batch size m and sample $\{x^i\}_{i=1}^m$ from the dataset and $\{z^i\}_{i=1}^m$ from ζ . Denote the generated samples by $y_\theta^i = g_\theta(z^i)$, and the empirical distributions by

$$\hat{\mathbf{x}} = \frac{1}{m} \sum_{i=1}^m \delta_{x^i}, \quad \hat{\mathbf{y}}_\theta = \frac{1}{m} \sum_{i=1}^m \delta_{y_\theta^i}.$$

The empirical distance $\mathcal{W}_{c+l, \varepsilon}(\hat{\mathbf{x}}, \hat{\mathbf{y}}_\theta)$ can be efficiently approximated by the Sinkhorn algorithm.

3.3 Reducing the bias with mixed Sinkhorn divergence

When implementing the Sinkhorn divergence (2.5) at the level of mini-batches, one canonical candidate clearly is

$$2\mathcal{W}_{c_\varphi, \varepsilon}(\hat{\mathbf{x}}, \hat{\mathbf{y}}_\theta) - \mathcal{W}_{c_\varphi, \varepsilon}(\hat{\mathbf{x}}, \hat{\mathbf{x}}) - \mathcal{W}_{c_\varphi, \varepsilon}(\hat{\mathbf{y}}_\theta, \hat{\mathbf{y}}_\theta), \quad (3.7)$$

which is indeed what is used in [19]. While the expression in (3.7) does converge in expectation to (2.5) for $m \rightarrow \infty$ ([20, Theorem 3]), it is not clear whether it is an adequate loss given data of fixed batch size m . In fact, we find that this is not the case, and demonstrate it here empirically.

Example 3.4. *We build an example where the data distribution μ belongs to a parameterized family of distributions $\{\nu_\theta\}_\theta$, with $\mu = \nu_{0.8}$ (details in Appendix A.3). As shown in Figure 1 (top two rows), neither the expected regularized distance (2.4) nor the Sinkhorn divergence (2.5) reaches minimum at $\theta = 0.8$, especially for small m . This means that optimizing ν over mini-batches will not lead to μ .*

Instead, we propose the following *mixed Sinkhorn divergence* at the level of mini-batches:

$$\widehat{\mathcal{W}}_{c, \varepsilon}^{\text{mix}}(\hat{\mathbf{x}}, \hat{\mathbf{x}}', \hat{\mathbf{y}}_\theta, \hat{\mathbf{y}}'_\theta) := \mathcal{W}_{c, \varepsilon}(\hat{\mathbf{x}}, \hat{\mathbf{y}}_\theta) + \mathcal{W}_{c, \varepsilon}(\hat{\mathbf{x}}', \hat{\mathbf{y}}'_\theta) - \mathcal{W}_{c, \varepsilon}(\hat{\mathbf{x}}, \hat{\mathbf{x}}') - \mathcal{W}_{c, \varepsilon}(\hat{\mathbf{y}}_\theta, \hat{\mathbf{y}}'_\theta), \quad (3.8)$$

where $\hat{\mathbf{x}}$ and $\hat{\mathbf{x}}'$ are the empirical distributions of mini-batches from the data distribution, and $\hat{\mathbf{y}}_\theta$ and $\hat{\mathbf{y}}'_\theta$ from the IGM distribution $\zeta \circ g^{-1}$. The idea is to take into account the bias within the distribution μ and that within the distribution ν_θ as well. The proposed divergence finds the correct minimizer for all m in Example 3.4 (Figure 1, bottom), and the improvement is not due solely to the double batch used by Equation (3.8). We further discuss this choice and our findings in Appendix A.3.

3.4 COT-GAN: Adversarial learning for sequential data

We now combine the results in Section 3.2 and Section 3.3 to formulate an adversarial training algorithm for IGMs. First, we approximate the set of functions (3.5) by truncating the sums at a fixed J , and we parameterize $\mathbf{h}_{\varphi_1} := (h_{\varphi_1}^j)_{j=1}^J$ and $\mathbf{M}_{\varphi_2} := (M_{\varphi_2}^j)_{j=1}^J$ as two separate neural networks, and let $\varphi := (\varphi_1, \varphi_2)$. To capture the adaptedness of those processes, we employ architectures where the output at time t depends on the input only up to time t . The mixed Sinkhorn divergence between $\hat{\mathbf{x}}$ and $\hat{\mathbf{y}}_\theta$ is then calculated with respect to a parameterized cost function

$$c_\varphi^{\mathcal{K}}(x, y) := c(x, y) + \sum_{j=1}^J \sum_{t=1}^{T-1} h_{\varphi_1, t}^j(y) \Delta_{t+1} M_{\varphi_2}^j(x). \quad (3.9)$$

Second, it is not obvious how to directly impose the martingale condition, as constraints involving conditional expectations cannot be easily enforced in practice. Rather, we penalize processes M for which increments at every time step are non-zero on average. For an $(\mathcal{X}, \mathcal{F}^{\mathcal{X}})$ -adapted process $M_{\varphi_2}^j$ and a mini-batch $\{x^i\}_{i=1}^m$ ($\sim \hat{\mathbf{x}}$), we define the martingale penalization for $\mathbf{M}_{\varphi_2} = (M_{\varphi_2}^j)_{j=1}^J$ as

$$p_{\mathbf{M}_{\varphi_2}}(\hat{\mathbf{x}}) := \frac{1}{mT} \sum_{j=1}^J \sum_{t=1}^{T-1} \left| \sum_{i=1}^m \frac{\Delta_{t+1} M_{\varphi_2}^j(x^i)}{\sqrt{\text{Var}[M_{\varphi_2}^j]} + \eta} \right|,$$

where $\text{Var}[M]$ is the empirical variance of M over time and batch, and $\eta > 0$ is a small constant. Third, we use the mixed normalization introduced in (3.8). Each of the four terms is approximated by running the Sinkhorn algorithm on the cost $c_\varphi^{\mathcal{K}}$ for L iterations.

Altogether, we arrive at the following adversarial objective function for COT-GAN:

$$\widehat{\mathcal{W}}_{c_\varphi^{\mathcal{K}}, \varepsilon}^{\text{mix}, L}(\hat{\mathbf{x}}, \hat{\mathbf{x}}', \hat{\mathbf{y}}_\theta, \hat{\mathbf{y}}'_\theta) - \lambda p_{\mathbf{M}_{\varphi_2}}(\hat{\mathbf{x}}), \quad (3.10)$$

where $\hat{\mathbf{x}}$ and $\hat{\mathbf{x}'}$ are empirical measures corresponding to non-overlapping subsets of the dataset, $\hat{\mathbf{y}}_\theta$ and $\hat{\mathbf{y}}'_\theta$ are the ones corresponding to two samples from ν_θ , and λ is a positive constant. We update θ to decrease this objective, and φ to increase it.

While the generator $g_\theta : \mathcal{Z} \rightarrow \mathcal{X}$ acts as in classical GANs, the adversarial role here is played by \mathbf{h}_{φ_1} and \mathbf{M}_{φ_2} . In this setting, the discriminator, parameterized by φ , learns a robust (worst-case) distance between the real data distribution μ and the generated distribution ν_θ , where the class of cost functions as in (3.9) originates from causality. The algorithm is summarized in Algorithm 1. Its time complexity scales as $\mathcal{O}((J + d)L T m^2)$ for each iteration.

4 Related work

Early video generation literature focuses on dynamic texture modeling [16, 35, 40]. Recent efforts in video generation within the GAN community have been devoted to designing GAN architectures of generator and discriminator to tackle the spatio-temporal dependencies separately, e.g., [39, 34, 36]. VGAN [39] explored a two-stream generator that combines a network for a static background and another one for moving foreground trained on the original GAN objective. TGAN [34] proposed a new structure capable of generating dynamic background as well as a weight clipping trick to regularize the discriminator. In addition to a unified generator, MoCoGAN [36] employed two discriminators to judge both the quality of frames locally and the evolution of motions globally.

The broader literature of sequential data generation attempts to capture the dependencies in time by simply deploying recurrent neural networks in the architecture [28, 18, 23, 42]. Among them, TimeGAN [42] demonstrated improvements in time series generation by adding a teacher-forcing component in the loss function. Alternatively, WaveGAN [15] adopted the causal structure of WaveNet [38]. Despite substantial progress made, existing sequential GANs are generally domain-specific. We therefore aim to offer a framework that considers (transport) causality in the objective function and is suitable for more general sequential settings.

Whilst our analysis is built upon [14] and [19], we remark two major differences between COT-GAN and the Sinkhorn GAN in [19]. First, we consider a different family of costs. While [19] learns the cost function $c(f_\varphi(x), f_\varphi(y))$ by parametrizing f with φ , the family of costs in COT-GAN is found by adding a causal component to $c(x, y)$ in terms of \mathbf{h}_{φ_1} and \mathbf{M}_{φ_2} . is the mixed Sinkhorn divergence we propose, which reduces biases in parameter estimation and can be used as a generic divergence for training IGMs not limited to time series settings.

Algorithm 1: training COT-GAN by SGD

Data: $\{x^i\}_{i=1}^N$ (real data), ζ (probability distribution on latent space \mathcal{Z})

Parameters: θ_0, φ_0, m (batch size), ε (regularization parameter), L (number of Sinkhorn iterations), α (learning rate), λ (martingale penalty coefficient)

Result: θ, φ

Initialize: $\theta \leftarrow \theta_0, \varphi \leftarrow \varphi_0$

for $k = 1, 2, \dots$ **do**

 Sample $\{x^i\}_{i=1}^m$ and $\{x'^i\}_{i=1}^m$ from real data;

 Sample $\{z^i\}_{i=1}^m$ and $\{z'^i\}_{i=1}^m$ from ζ ;

$(y_\theta^i, y_\theta'^i) \leftarrow (g_\theta(z^i), g_\theta(z'^i))$;

 compute $\widehat{\mathcal{W}}_{c_\varphi^\mathcal{K}, \varepsilon}^{\text{mix}, L}(\hat{\mathbf{x}}, \hat{\mathbf{x}}', \hat{\mathbf{y}}_\theta, \hat{\mathbf{y}}_\theta')$ (3.8) by the Sinkhorn algorithm, with $c_\varphi^\mathcal{K}$ given by (3.9)

$\varphi \leftarrow \varphi + \alpha \nabla_\varphi \left(\widehat{\mathcal{W}}_{c_\varphi^\mathcal{K}, \varepsilon}^{\text{mix}, L}(\hat{\mathbf{x}}, \hat{\mathbf{x}}', \hat{\mathbf{y}}_\theta, \hat{\mathbf{y}}_\theta') - \lambda p_{\mathbf{M}_{\varphi_2}}(\hat{\mathbf{x}}) \right)$

 Sample $\{x^i\}_{i=1}^m$ and $\{x'^i\}_{i=1}^m$ from real data;

 Sample $\{z^i\}_{i=1}^m$ and $\{z'^i\}_{i=1}^m$ from ζ ;

$(y_\theta^i, y_\theta'^i) \leftarrow (g_\theta(z^i), g_\theta(z'^i))$;

 compute $\widehat{\mathcal{W}}_{c_\varphi^\mathcal{K}, \varepsilon}^{\text{mix}, L}(\hat{\mathbf{x}}, \hat{\mathbf{x}}', \hat{\mathbf{y}}_\theta, \hat{\mathbf{y}}_\theta')$ (3.8) by the Sinkhorn algorithm, with $c_\varphi^\mathcal{K}$ given by (3.9)

$\theta \leftarrow \theta - \alpha \nabla_\theta \left(\widehat{\mathcal{W}}_{c_\varphi^\mathcal{K}, \varepsilon}^{\text{mix}, L}(\hat{\mathbf{x}}, \hat{\mathbf{x}}', \hat{\mathbf{y}}_\theta, \hat{\mathbf{y}}_\theta') \right)$;

end

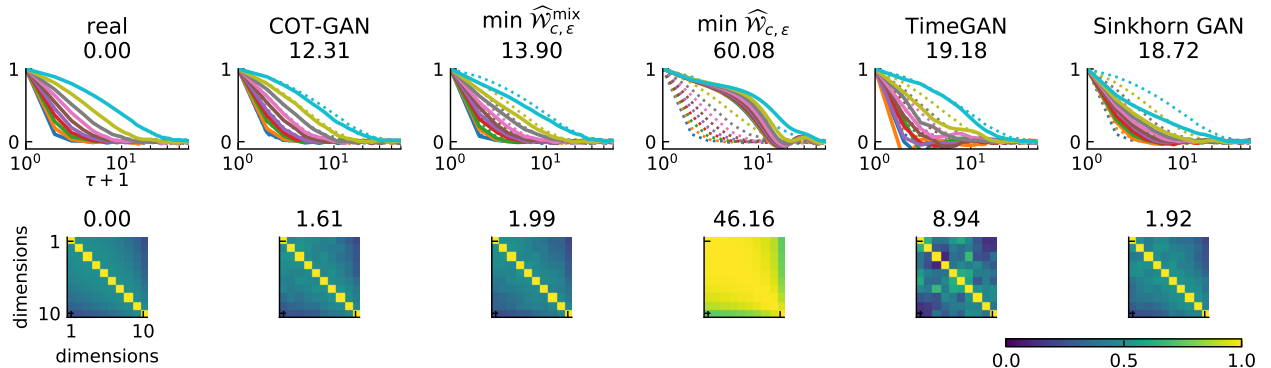


Figure 2: Results on learning the multivariate AR-1 process. Top row shows the auto-correlation coefficient for each channel. Bottom row shows the correlation coefficient between channels averaged over time. The number on top of each panel is the sum of the absolute difference between the correlation coefficients computed from real (leftmost) and generated samples.

5 Experiments

5.1 Time series

We now validate COT-GAN empirically². For times series that have a relatively small dimensionality d but exhibit complex temporal structure, we compare COT-GAN with the following methods: **Direct minimization** of Sinkhorn divergences $\widehat{\mathcal{W}}_{c, \varepsilon}^{\text{mix}}$ (3.8) and $\widehat{\mathcal{W}}_{c, \varepsilon}$ (3.7); **TimeGAN** [42] as reviewed in Section 4; **Sinkhorn GAN**, similar to [19] with cost $c(f_\varphi(x), f_\varphi(y))$ where φ is trained to increase the mixed Sinkhorn divergence with weight clipping. All methods use $c(x, y) = \|x - y\|_2^2$. The networks h and M in COT-GAN and f in Sinkhorn GAN share the same architecture. Details of models and datasets are in Appendix B.1.

Autoregressive processes. We first test whether COT-GAN can learn temporal and spatial correlation in a multivariate first-order auto-regressive process (AR-1). Results are shown in Figure 2. COT-GAN samples have correlation structures

²Code and data are available at github.com/neuripss2020/COT-GAN

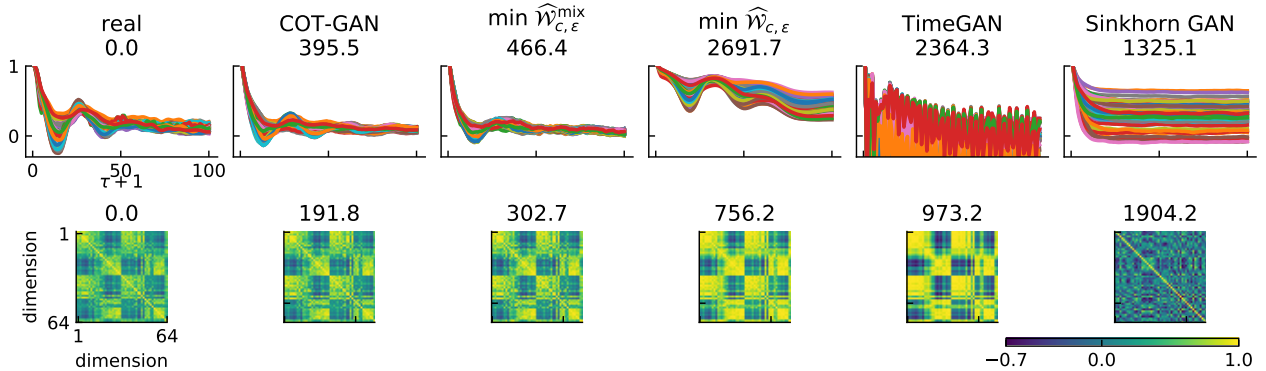


Figure 3: Results on EEG data. The same correlations as Figure 2 are shown.

that best match the real data. Minimizing the mixed divergence produces almost as good correlations as COT-GAN, but with less accurate auto-correlation. Minimizing the original Sinkhorn divergence yields poor results, and neither TimeGAN nor Sinkhorn GAN could capture the correlation structure for this dataset.

Noisy oscillations. The noisy oscillation distribution is composed of sequences of 20-element arrays (1-D images) [41]. Figure 6 in Appendix B.1 shows data as well as generated samples by different training methods. To evaluate performance, we estimate two attributes of the samples by Monte Carlo: the marginal distribution of pixel values, and the joint distribution of the location at adjacent time steps. COT-GAN samples match the real data best.

Electroencephalography (EEG). This dataset is from the UCI repository [17] and contains recordings from 43 healthy subjects each undergoing around 80 trials. Each data sequence has 64 channels and we model the first 100 time steps. We trained and evaluated each method 16 times with different training and test splits. We evaluated performance by the maximum mean discrepancy (MMD), and the match with data in terms of temporal and channel correlations, and frequency spectrum. In addition, we investigated how the coefficient λ affects sample quality. We show an example of the data and learned correlations in Figure 3, and summary statistics of all evaluation metrics in Figure 8 in Appendix B.1. COT-GANs generate the best samples compared with other baselines across all four metrics. A smaller λ tends to generate less realistic correlation patterns, but slightly better match in frequency spectrum.

5.2 Videos

We train COT-GAN on Sprites animations [27, 33] and human action sequences [11], and compare with MoCoGAN [36]. The evaluation metrics are Fréchet Inception Distance (FID) [24] comparing individual frames, Fréchet Video Distance (FVD) [37] which compares the video sequences as a whole by mapping samples into features via pretrained 3D convolutional networks, and their kernel counterparts (KID, KVD) [10]. Previous studies suggest that FVD correlates better with human judgement than KVD for videos [37], whereas KID does so better than FID on images [44].

We pre-process the Sprites and human action sequences to have a sequence length of $T = 13$ and $T = 16$, respectively. Each frame has dimension $64 \times 64 \times 3$. We employ the same architecture of generator and discriminator to train both datasets. Both the generator and discriminator comprises generic LSTM with 2-D convolutional layers. The detailed data pre-processing, GAN architectures, hyper-parameter settings, and training techniques are reported in Appendix B.2. We show the real data and samples from COT-GAN side by side in Figure 4.

Table 1: Evaluations for video datasets. Lower value means better sample quality.

Sprites	FVD	FID	KVD	KID
MoCoGAN	1213.2	281.3	160.1	0.33
COT-GAN	444.6	83.5	64.0	0.077
Human actions				
MoCoGAN	661.8	128.4	60.4	0.21
COT-GAN	541.0	52.4	46.2	0.096

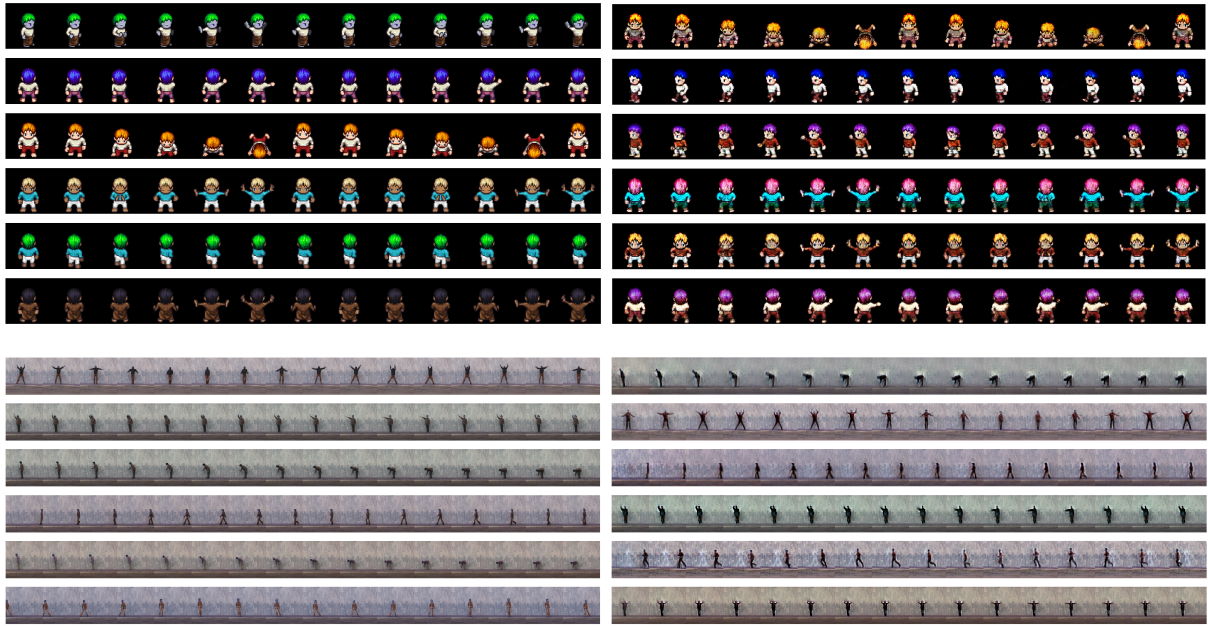


Figure 4: Animated (top) and human (bottom) action videos. Left column reports real data samples, and right column samples from COT-GAN.

The evaluation scores in Table 1 are estimated using 5000 generated samples. COT-GAN is the better performing method in both tasks for all four measurements. Further samples, and comparison with direct minimization of the mixed Sinkhorn divergence, are provided in Appendix C.

6 Discussion

The performance of COT-GAN suggests that constraining the transport plans to be causal is a promising direction for generating sequential data. The approximations we introduce, such as the mixed Sinkhorn distance (3.8) and truncated sum in (3.5), are sufficient to produce good experimental results, and provide opportunities for more theoretical analyses in future studies. Directions of future development include ways to learn from data with flexible lengths, extensions to conditional COT-GAN, and improved methods to enforce the martingale property for M and better parameterize the causality constraint.

References

- [1] Acciaio, B., Backhoff-Veraguas, J., and Carmona, R. Extended mean field control problems: stochastic maximum principle and transport perspective. *SIAM Journal on Control and Optimization*, 57(6), 2019.
- [2] Acciaio, B., Backhoff-Veraguas, J., and Zalashko, A. Causal optimal transport and its links to enlargement of filtrations and continuous-time stochastic optimization. *Stochastic Processes and their Applications*, 2019.
- [3] Acciaio, B., Backhoff-Veraguas, J., and Jia, J. Cournot-nash equilibrium and optimal transport in a dynamic setting. *arXiv preprint arXiv:2002.08786*, 2020.
- [4] Arbel, M., Sutherland, D., Bińkowski, M., and Gretton, A. On gradient regularizers for mmd gans. In *NeurIPS*, 2018.
- [5] Arjovsky, M. and Bottou, L. Towards principled methods for training generative adversarial networks. arxiv e-prints, art. *arXiv preprint arXiv:1701.04862*, 2017.
- [6] Arjovsky, M., Chintala, S., and Bottou, L. Wasserstein generative adversarial networks. In *ICML*, 2017.
- [7] Backhoff, J., Beiglbock, M., Lin, Y., and Zalashko, A. Causal transport in discrete time and applications. *SIAM Journal on Optimization*, 27(4), 2017.
- [8] Backhoff, J., Bartl, D., Beiglbock, M., and Wiesel, J. Estimating processes in adapted Wasserstein distance. *arXiv preprint arXiv:2002.07261*, 2020.

- [9] Backhoff-Veraguas, J., Bartl, D., Beiglböck, M., and Eder, M. Adapted Wasserstein distances and stability in mathematical finance. *arXiv preprint arXiv:1901.07450*, 2019.
- [10] Bińkowski, M., Sutherland, D. J., Arbel, M., and Gretton, A. Demystifying mmd gans. *arXiv preprint arXiv:1801.01401*, 2018.
- [11] Blank, M., Gorelick, L., Shechtman, E., Irani, M., and Basri, R. Actions as space-time shapes. In *ICCV*, 2005.
- [12] Bousquet, O., Gelly, S., Tolstikhin, I., Simon-Gabriel, C.-J., and Schoelkopf, B. From optimal transport to generative modeling: the vegan cookbook. *arXiv preprint arXiv:1705.07642*, 2017.
- [13] Cover, T. M. and Thomas, J. A. *Elements of information theory*. John Wiley & Sons, 2012.
- [14] Cuturi, M. Sinkhorn distances: Lightspeed computation of optimal transport. In *NeurIPS*, 2013.
- [15] Donahue, C., McAuley, J. J., and Puckette, M. S. Adversarial audio synthesis. In *ICLR*, 2019.
- [16] Doretto, G., Chiuso, A., Wu, Y. N., and Soatto, S. Dynamic textures. *International Journal of Computer Vision*, 51(2), 2003.
- [17] Dua, D. and Graff, C. UCI machine learning repository, 2017. URL <http://archive.ics.uci.edu/ml>.
- [18] Esteban, C., Hyland, S. L., and Rätsch, G. Real-valued (medical) time series generation with recurrent conditional gans. *arXiv preprint arXiv:1706.02633*, 2017.
- [19] Genevay, A., Peyre, G., and Cuturi, M. Learning generative models with sinkhorn divergences. In *AISTATS*, 2018.
- [20] Genevay, A., Chizat, L., Bach, F., Cuturi, M., and Peyré, G. Sample complexity of sinkhorn divergences. In *AISTATS*, 2019.
- [21] Good, I. J. et al. Maximum entropy for hypothesis formulation, especially for multidimensional contingency tables. *The Annals of Mathematical Statistics*, 34(3), 1963.
- [22] Goodfellow, I., Pouget-Abadie, J., Mirza, M., Xu, B., Warde-Farley, D., Ozair, S., Courville, A., and Bengio, Y. Generative adversarial nets. In *NeurIPS*, 2014.
- [23] Haradal, S., Hayashi, H., and Uchida, S. Biosignal data augmentation based on generative adversarial networks. In *International Conference in Medicine and Biology Society*, 2018.
- [24] Heusel, M., Ramsauer, H., Unterthiner, T., Nessler, B., and Hochreiter, S. Gans trained by a two time-scale update rule converge to a local nash equilibrium. In *NeurIPS*, 2017.
- [25] Johnson, M. J., Duvenaud, D. K., Wiltschko, A., Adams, R. P., and Datta, S. R. Composing graphical models with neural networks for structured representations and fast inference. In *Advances in neural information processing systems*, pp. 2946–2954, 2016.
- [26] Li, C.-L., Chang, W.-C., Cheng, Y., Yang, Y., and Póczos, B. Mmd gan: Towards deeper understanding of moment matching network. In *NeurIPS*, 2017.
- [27] Li, Y. and Mandt, S. Disentangled sequential autoencoder. *arXiv preprint arXiv:1803.02991*, 2018.
- [28] Mogren, O. C-rnn-gan: Continuous recurrent neural networks with adversarial training. *arXiv preprint arXiv:1611.09904*, 2016.
- [29] Mroueh, Y., Li, C.-L., Sercu, T., Raj, A., and Cheng, Y. Sobolev gan. In *ICLR*, 2018.
- [30] Nowozin, S., Cseke, B., and Tomioka, R. f-gan: Training generative neural samplers using variational divergence minimization. In *NeurIPS*, 2016.
- [31] Orlin, J. B. A faster strongly polynomial minimum cost flow algorithm. *Operations research*, 41(2):338–350, 1993.
- [32] Pele, O. and Werman, M. Fast and robust earth mover’s distances. In *2009 IEEE 12th International Conference on Computer Vision*, pp. 460–467. IEEE, 2009.
- [33] Reed, S. E., Zhang, Y., Zhang, Y., and Lee, H. Deep visual analogy-making. In *NeurIPS*, 2015.
- [34] Saito, M., Matsumoto, E., and Saito, S. Temporal generative adversarial nets with singular value clipping. In *ICCV*, 2017.
- [35] Szummer, M. and Picard, R. W. Temporal texture modeling. In *International Conference on Image Processing*, volume 3, 1996.
- [36] Tulyakov, S., Liu, M.-Y., Yang, X., and Kautz, J. Mocogan: Decomposing motion and content for video generation. In *CVPR*, 2018.
- [37] Unterthiner, T., van Steenkiste, S., Kurach, K., Marinier, R., Michalski, M., and Gelly, S. Fvd: A new metric for video generation. 2019.

- [38] van den Oord, A., Dieleman, S., Zen, H., Simonyan, K., Vinyals, O., Graves, A., Kalchbrenner, N., Senior, A. W., and Kavukcuoglu, K. Wavenet: A generative model for raw audio. In *ISCA workshop*, 2016.
- [39] Vondrick, C., Pirsiaavash, H., and Torralba, A. Generating videos with scene dynamics. In *NeurIPS*, 2016.
- [40] Wei, L.-Y. and Levoy, M. Fast texture synthesis using tree-structured vector quantization. In *Annual conference on Computer graphics and interactive techniques*, 2000.
- [41] Wenliang, L. K. and Sahani, M. A neurally plausible model for online recognition and postdiction in a dynamical environment. In *NeurIPS*. 2019.
- [42] Yoon, J., Jarrett, D., and van der Schaar, M. Time-series generative adversarial networks. In *NeurIPS*. 2019.
- [43] Zhang, X. L., Begleiter, H., Porjesz, B., Wang, W., and Litke, A. Event related potentials during object recognition tasks. *Brain Research Bulletin*, 38(6), 1995.
- [44] Zhou, S., Gordon, M., Krishna, R., Narcomey, A., Fei-Fei, L. F., and Bernstein, M. Hype: A benchmark for human eye perceptual evaluation of generative models. In *NeurIPS*, 2019.

COT-GAN: Generating Sequential Data via Causal Optimal Transport

Supplementary material

A Specifics on regularized Causal Optimal Transport

A.1 Limits of regularized Causal Optimal Transport

In this section we prove the limits stated in Remark 3.2.

Lemma A.1. *Let μ and ν be discrete measures, say on path spaces \mathbb{X}^T and \mathbb{Y}^T , with $|\mathbb{X}| = m$ and $|\mathbb{Y}| = n$. Then*

$$\mathcal{K}_{c,\varepsilon}(\mu, \nu) \xrightarrow{\varepsilon \rightarrow 0} \mathcal{K}_c(\mu, \nu).$$

Proof. We mimic the proof of Theorem 4.5 in [3], and note that the entropy of any $\pi \in \Pi(\mu, \nu)$ is uniformly bounded:

$$0 \leq H(\pi) \leq C := m^T n^T e^{-1}. \quad (\text{A.1})$$

This yields

$$\begin{aligned} \inf_{\pi \in \Pi^{\mathcal{K}}(\mu, \nu)} \mathbb{E}^{\pi}[c] - \varepsilon C + \varepsilon H(\pi_{c,\varepsilon}^{\mathcal{K}}(\mu, \nu)) &\leq \inf_{\pi \in \Pi^{\mathcal{K}}(\mu, \nu)} \{\mathbb{E}^{\pi}[c] - \varepsilon H(\pi)\} + \varepsilon H(\pi_{c,\varepsilon}^{\mathcal{K}}(\mu, \nu)) \\ &\leq \inf_{\pi \in \Pi^{\mathcal{K}}(\mu, \nu)} \mathbb{E}^{\pi}[c] + \varepsilon H(\pi_{c,\varepsilon}^{\mathcal{K}}(\mu, \nu)). \end{aligned} \quad (\text{A.2})$$

Now, note that $\inf_{\pi \in \Pi^{\mathcal{K}}(\mu, \nu)} \{\mathbb{E}^{\pi}[c] - \varepsilon H(\pi)\} = \mathcal{K}_{c,\varepsilon}(\mu, \nu) - \varepsilon H(\pi_{c,\varepsilon}^{\mathcal{K}}(\mu, \nu))$, and that, for $\varepsilon \rightarrow 0$, the LHS and RHS in (A.2) both tend to $\mathcal{K}_c(\mu, \nu)$. \square

Lemma A.2. *Let μ and ν be discrete measures. Then*

$$\mathcal{K}_{c,\varepsilon}(\mu, \nu) \xrightarrow{\varepsilon \rightarrow \infty} \mathbb{E}^{\mu \otimes \nu}[c(x, y)].$$

Proof. Being μ and ν discrete, $\mathbb{E}^{\pi}[c]$ is uniformly bounded for $\pi \in \Pi^{\mathcal{K}}(\mu, \nu)$. Therefore, for ε big enough, the optimizer in $\mathcal{P}_{c,\varepsilon}^{\mathcal{K}}(\mu, \nu)$ is $\hat{\pi} := \operatorname{argmax}_{\pi \in \Pi^{\mathcal{K}}(\mu, \nu)} H(\pi) = \mu \otimes \nu$, the independent coupling, for which $H(\mu \otimes \nu) = H(\mu) + H(\nu)$; see [13] and [21]. Therefore, for ε big enough, we have $\mathcal{K}_{c,\varepsilon}(\mu, \nu) = \mathbb{E}^{\mu \otimes \nu}[c(x, y)]$. \square

A.2 Reformulation of the COT problem

Proof. The causal constraint (3.2) can be expressed using the following characteristic function:

$$\sup_{l \in \mathcal{L}(\mu)} \mathbb{E}^{\pi}[l(x, y)] = \begin{cases} 0 & \text{if } \pi \text{ is causal;} \\ +\infty & \text{otherwise.} \end{cases} \quad (\text{A.3})$$

This allows to rewrite (3.3) as

$$\begin{aligned} \mathcal{P}_{c,\varepsilon}^{\mathcal{K}}(\mu, \nu) &= \inf_{\pi \in \Pi(\mu, \nu)} \left\{ \mathbb{E}^{\pi}[c(x, y)] - \varepsilon H(\pi) + \sup_{l \in \mathcal{L}(\mu)} \mathbb{E}^{\pi}[l(x, y)] \right\} \\ &= \inf_{\pi \in \Pi(\mu, \nu)} \sup_{l \in \mathcal{L}(\mu)} \{\mathbb{E}^{\pi}[c(x, y) + l(x, y)] - \varepsilon H(\pi)\} \\ &= \sup_{l \in \mathcal{L}(\mu)} \inf_{\pi \in \Pi(\mu, \nu)} \{\mathbb{E}^{\pi}[c(x, y) + l(x, y)] - \varepsilon H(\pi)\} \\ &= \sup_{l \in \mathcal{L}(\mu)} \mathcal{P}_{c+l, \varepsilon}(\mu, \nu), \end{aligned}$$

where the third equality holds by the min-max theorem, thanks to convexity of $\mathcal{L}(\mu)$, and convexity and compactness of $\Pi(\mu, \nu)$. \square

A.3 Sinkhorn divergence at the level of mini-batches

Empirical observation of the bias in Example 3.4. In the experiment mentioned in Example 3.4, we consider a set of distributions ν 's as sinusoids with random phase, frequency and amplitude. We let μ be one element in this set whose amplitude is uniformly distributed between minimum 0.3 and maximum 0.8. On the other hand, for each ν , the amplitude is uniformly distributed between the same minimum 0.3 and a maximum that lies in $\{0.4, 0.5, \dots, 1.2\}$. Thus, the only parameter of the distribution being varied is the maximum amplitude. We may equivalently take the maximum amplitude as a single θ that parameterizes ν_θ , so that $\mu = \nu_{0.8}$. Figure 1 illustrates that the sample Sinkhorn divergence (3.7) (or regularized distance (2.4)) does not recover the optimizer 0.8, while the proposed mix Sinkhorn divergence (3.8) does.

Further discussion. As mentioned in Section 3.3, when implementing the Sinkhorn divergence (2.5) at the level of mini-batches, one canonical choice is the one adopted in [19], that is

$$2\mathcal{W}_{c_\varphi, \varepsilon}(\hat{\mathbf{x}}, \hat{\mathbf{y}}_\theta) - \mathcal{W}_{c_\varphi, \varepsilon}(\hat{\mathbf{x}}, \hat{\mathbf{x}}) - \mathcal{W}_{c_\varphi, \varepsilon}(\hat{\mathbf{y}}_\theta, \hat{\mathbf{y}}_\theta). \quad (\text{A.4})$$

What inspired us the different choice of the mixed Sinkhorn divergence in (3.8), that is

$$\mathcal{W}_{c_\varphi, \varepsilon}(\hat{\mathbf{x}}, \hat{\mathbf{y}}_\theta) + \mathcal{W}_{c_\varphi, \varepsilon}(\hat{\mathbf{x}}', \hat{\mathbf{y}}'_\theta) - \mathcal{W}_{c_\varphi, \varepsilon}(\hat{\mathbf{x}}, \hat{\mathbf{x}}') - \mathcal{W}_{c_\varphi, \varepsilon}(\hat{\mathbf{y}}_\theta, \hat{\mathbf{y}}'_\theta), \quad (\text{A.5})$$

is the idea of also taking into account the bias within the distribution μ and that within the distribution ν_θ , when sampling mini-batches from them.

Clearly, when the batch size $m \rightarrow \infty$, both (A.4) and (A.5) converge to (2.5) in expectation, see [20, Theorem 3]. So the main point here is, for a fixed $m \in \mathbb{N}$, which one of the two does a better job in translating the idea of the Sinkhorn divergence at the level of mini-batches. Experiments suggest that (A.5) is indeed the better choice. To support this fact, note that the triangular inequality implies

$$\mathbb{E} [|\mathcal{W}_{c_\varphi, \varepsilon}(\hat{\mathbf{x}}, \hat{\mathbf{y}}_\theta) + \mathcal{W}_{c_\varphi, \varepsilon}(\hat{\mathbf{x}}', \hat{\mathbf{y}}'_\theta) - 2\mathcal{W}_{c_\varepsilon}(\mu, \nu)|] \leq 2\mathbb{E} [|\mathcal{W}_{c_\varphi, \varepsilon}(\hat{\mathbf{x}}, \hat{\mathbf{y}}_\theta) - \mathcal{W}_{c_\varepsilon}(\mu, \nu)|].$$

One can possibly argue that in (A.5) we are using two batches of size m , thus simply considering a bigger mini-batch, say of size $2m$, may perform as well. However, we have considered this case and our experiments confirm that the mixed Sinkhorn divergence (A.5) we suggest does perform better than the so-far used (A.4) even when in the latter we allow for bigger batch size. This reasoning can be pushed further, by for example considering $\mathcal{W}_{c_\varphi, \varepsilon}(\cdot, \cdot)$ for all four combinations of samples with and without $'$. Implementations showed that there is no advantage in doing so while requiring more computations.

The MMD limiting case. In the limit $\varepsilon \rightarrow \infty$, Genevay et al. [19] showed that $\mathcal{W}_{c_\varepsilon}(\mu, \nu) \rightarrow \text{MMD}_{-c}(\mu, \nu)$ under the kernel defined by $-c(x, y)$. Here we want to point out an interesting fact about the limiting behavior of the mixed Sinkhorn divergence.

Remark A.3. *Given distributions of mini-batches $\hat{\mathbf{x}}$ and $\hat{\mathbf{y}}$ formed by samples from μ and ν , respectively, in the limit $\varepsilon \rightarrow \infty$, the Sinkhorn divergence $\widehat{\mathcal{W}}_{c_\varepsilon}(\hat{\mathbf{x}}, \hat{\mathbf{y}})$ converges to a biased estimator of $\text{MMD}_{-c}(\mu, \nu)$; given additional $\hat{\mathbf{x}}'$ and $\hat{\mathbf{y}}'$ from μ and ν , respectively, the mixed Sinkhorn divergence $\widehat{\mathcal{W}}_{c_\varepsilon}^{\text{mix}}(\hat{\mathbf{x}}, \hat{\mathbf{x}}', \hat{\mathbf{y}}, \hat{\mathbf{y}}')$ converges to an unbiased estimator of $\text{MMD}_{-c}(\mu, \nu)$.*

Proof. The first part of the statement relies on the fact that $\text{MMD}_{-c}(\hat{\mathbf{x}}, \hat{\mathbf{y}})$ is a biased estimator of $\text{MMD}_{-c}(\mu, \nu)$. Indeed, we have

$$\widehat{\mathcal{W}}_{c_\varepsilon}(\hat{\mathbf{x}}, \hat{\mathbf{y}}) \xrightarrow{\varepsilon \rightarrow \infty} \text{MMD}_{-c}(\hat{\mathbf{x}}, \hat{\mathbf{y}}) = -\frac{1}{m^2} \sum_{i=1}^m \sum_{j=1}^m [c(x^i, x^j) + c(y^i, y^j) - 2c(x^i, y^j)].$$

Now note that

$$\begin{aligned} \frac{1}{m^2} \sum_{i=1}^m \sum_{j=1}^m \mathbb{E}[c(x^i, x^j)] &= \frac{1}{m^2} \left[\sum_{i=1}^m \mathbb{E}_\mu[c(x^i, x^i)] + \sum_{i \neq j} \mathbb{E}_{\mu \otimes \mu}[c(x^i, x^j)] \right] \\ &= \frac{m-1}{m} \mathbb{E}_{\mu \otimes \mu}[c(x, x')], \end{aligned}$$

where we have used the fact that $c(x^i, x^i) = 0$. A similar result holds for the sum over $c(y^i, y^j)$. On the other hand, $\frac{1}{m^2} \sum_{ij} \mathbb{E}[c(x^i, y^j)] = \mathbb{E}_{\mu \otimes \nu}[c(x, y)]$. Therefore

$$\begin{aligned}\mathbb{E} \text{MMD}_{-c}(\hat{\mathbf{x}}, \hat{\mathbf{y}}) &= -\frac{m-1}{m} [\mathbb{E}_{\mu \otimes \mu}[c(x, x')] + \mathbb{E}_{\nu \otimes \nu}[c(y, y')]] + 2\mathbb{E}_{\mu \otimes \nu}[c(x, y)] \\ &\neq \text{MMD}_{-c}(\mu, \nu),\end{aligned}$$

which completes the proof of the first part of the statement.

For the second part, note that $\mathcal{W}_{c, \varepsilon}(\mu, \nu) \rightarrow \mathbb{E}_{\mu \otimes \mu}[c(x, x')]$ as $\varepsilon \rightarrow \infty$ [19, Theorem 1], thus

$$\begin{aligned}\widehat{\mathcal{W}}_{c, \varepsilon}^{\text{mix}}(\hat{\mathbf{x}}, \hat{\mathbf{x}}', \hat{\mathbf{y}}, \hat{\mathbf{y}}') &\rightarrow \mathbb{E}_{\hat{\mathbf{x}} \otimes \hat{\mathbf{y}}}[c(x, y)] + \mathbb{E}_{\hat{\mathbf{x}}' \otimes \hat{\mathbf{y}}'}[c(x', y')] - \mathbb{E}_{\hat{\mathbf{x}} \otimes \hat{\mathbf{x}}'}[c(x, x')] - \mathbb{E}_{\hat{\mathbf{y}} \otimes \hat{\mathbf{y}}'}[c(y, y')] \\ &= \frac{1}{m^2} \sum_{i=1}^m \sum_{j=1}^m [c(x^i, y^i) + c(x'^i, y'^i) - c(x^i, x'^i) - c(y^i, y'^i)].\end{aligned}$$

The RHS is an unbiased estimator of MMD, since its expectation is

$$\mathbb{E}_{\mu \otimes \nu}[c(x, y)] + \mathbb{E}_{\mu \otimes \nu}[c(x', y')] - \mathbb{E}_{\mu \otimes \mu}[c(x, x')] - \mathbb{E}_{\nu \otimes \nu}[c(y, y')] = \text{MMD}_{-c}(\mu, \nu).$$

□

Note that the bias refers to the parameter estimate, rather than the divergence itself. The mixed divergence may still be a biased estimate of the true Sinkhorn divergence. However, in the experiment of Example 3.4 we note that the minimum is reached for the parameter θ close to the real one (Figure 1, bottom). We defer detailed analysis of mixed divergence to a future paper.

B Experimental details

B.1 Low dimensional time series

Here we describe details of the experiments in Section 5.1.

Autoregressive process. The generative process to obtain data \mathbf{x}_t for the autoregressive process is

$$\mathbf{x}_t = \mathbf{A}\mathbf{x}_{t-1} + \zeta_t, \quad \zeta_t \stackrel{\text{i.i.d.}}{\sim} \mathcal{N}(0, \Sigma), \quad \Sigma = 0.5\mathbf{I} + 0.5,$$

where \mathbf{A} is diagonal with ten values evenly spaced between 0.1 and 0.9. We initialize \mathbf{x}_0 from a 10-dimensional standard normal, and ignore the data in the first 10 time steps so that the data sequence begins with a more or less stationary distribution. We use $\lambda = 0.1$ and $\varepsilon = 10.0$ for this experiment. Real data and generated samples are shown in Figure 5.

Noisy oscillation. This dataset comprises paths simulated from a noisy, nonlinear dynamical system. Each path is represented as a sequence of d -dimensional arrays, T time steps long, and can be displayed as a $d \times T$ -pixel image for visualization. At each discrete time step $t \in \{1, \dots, T\}$, data at time t , given by $\mathbf{x}_t \in [0, 1]^d$, is determined by the position of a “particle” following noisy, nonlinear dynamics. When shown as an image, each sample path appears visually as a “bump” travelling rightward, moving up and down in a zig-zag pattern as shown in Figure 6 (top left).

More precisely, the state of the particle at time t is described by its position and velocity $\mathbf{s}_t = (s_{t,1}, s_{t,2}) \in \mathbb{R}^2$, and evolves according to

$$\begin{aligned}\mathbf{s}_t &= \mathbf{f}(\mathbf{s}_{t-1}) + \zeta_t, \quad \zeta_t = \mathcal{N}(0, 0.1\mathbf{I}), \\ \mathbf{f}(\mathbf{s}_{t-1}) &= c_t \mathbf{A} \mathbf{s}_{t-1}; \quad c_t = \frac{1}{\|\mathbf{s}_{t-1}\|_2 \exp(-4(\|\mathbf{s}_{t-1}\|_2 - 0.3) + 1)},\end{aligned}$$

where $\mathbf{A} \in \mathbb{R}^{2 \times 2}$ is a rotation matrix, and \mathbf{s}_0 is uniformly distributed on the unit circle.

We take $T = 48$ and $d = 20$ so that \mathbf{x}_t is a vector of evaluations of a Gaussian function at 20 evenly spaced locations, and the peak of the Gaussian function follows the position of the particle $s_{t,1}$ for each t :

$$x_{t,i} = \exp \left[-\frac{(\text{loc}(i) - s_{t,1})^2}{2 \times 0.3^2} \right],$$

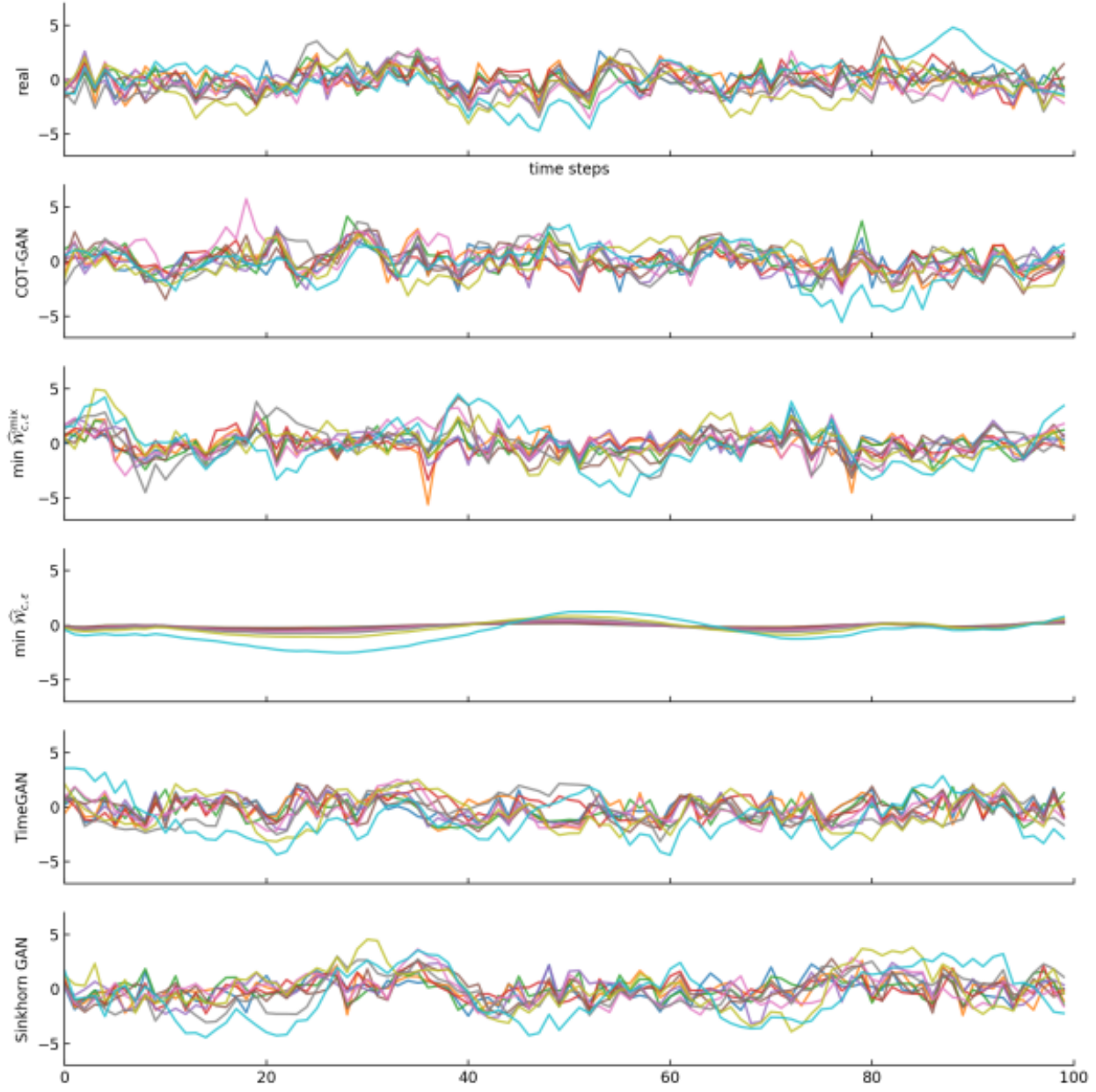


Figure 5: Data and samples obtained by different methods for the autoregressive process.

where $\text{loc} : \{1, \dots, d\} \rightarrow \mathbb{R}$ maps pixel indices to a grid of evenly spaced points in the space of particle position. Thus, \mathbf{x}_t , the observation at time t , contains information about $s_{t,1}$ but not $s_{t,2}$. A similar data generating process was used in [41], inspired by Johnson et al. [25].

We compare the marginal distribution of the pixel values $x_{t,i}$ and joint distribution of the bump location ($\text{argmax}_i x_{t,i}$) between adjacent time steps. See Figure 6.

Electroencephalography. We obtained EEG dataset from [43] and took the recordings of all the 43 subjects in the control group under the matching condition (S2). For each subject, we choose 75% of the trials as training data and the remaining for evaluation, giving 2841 training sequences and 969 test sequences in total. All data are subtracted by channel-wise mean, divided by three times the channel-wise standard deviation, and then passed through a tanh nonlinearity. We train and evaluate models 16 times with different splittings. For COT-GAN, we trained three variants

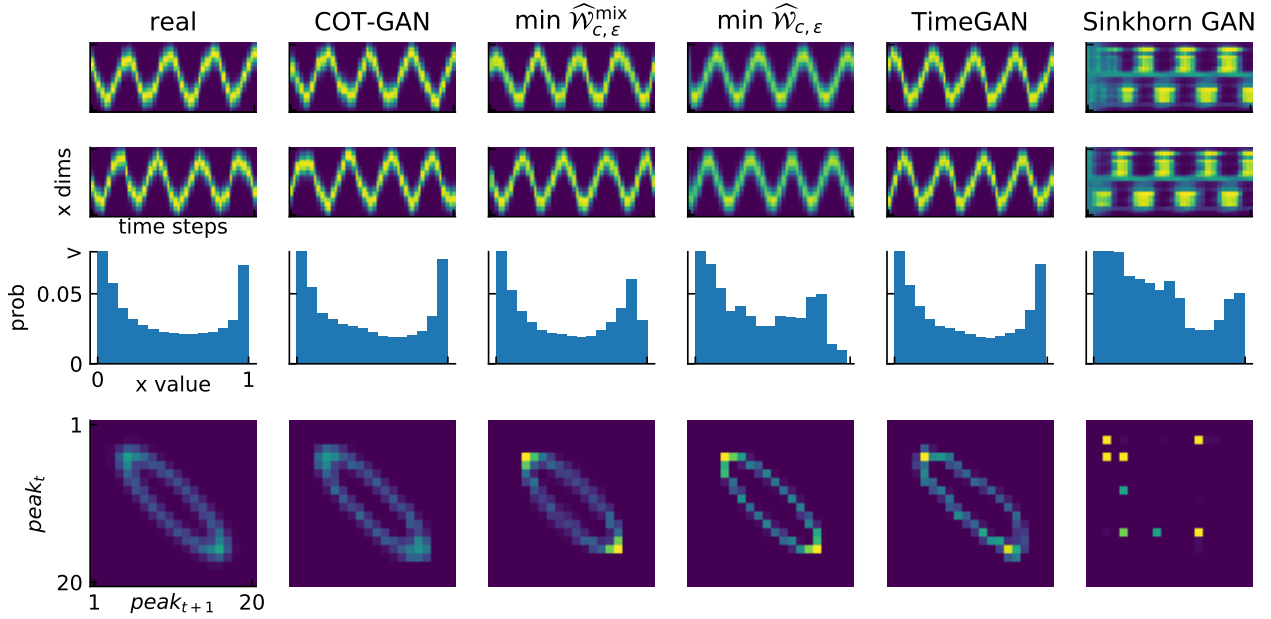


Figure 6: 1-D noisy oscillation. Top two rows show two samples from the data distribution and generators trained by different methods. Third row shows marginal distribution of pixels values (y axis clipped at 0.07 for clarity). Bottom row shows joint distribution of the position of the oscillation at adjacent time steps.

corresponding to λ being one of $\{1.0, 0.1, 0.01\}$, and $\epsilon = 100.0$ for all OT-based methods. Data and samples are shown in Figure 7.

We use four different metrics to compare sample quality. Relative MMD test that compares a test statistic based on $\text{MMD}(\mathcal{D}_{\text{real}}, \mathcal{D}_{\text{alternative}}) - \text{MMD}(\mathcal{D}_{\text{real}}, \mathcal{D}_{\text{COT-GAN } \lambda=1.0})$, where $\mathcal{D}_{\text{real}}$ indicates the real test dataset, $\mathcal{D}_{\text{COT-GAN } \lambda=1.0}$ is sampled from a COT-GAN with $\lambda = 1.0$, and $\mathcal{D}_{\text{alternative}}$ is sampled from an alternative method that is one of the following: COT-GAN with $\lambda \in \{0.1, 0.01\}$, direct minimizations of mixed and original Sinkhorn divergences, TimeGAN and Sinkhorn GAN. A larger value of the test statistic indicates that COT-GAN with $\lambda = 1.0$ is better compared to the alternative. We do not employ the hypothesis testing framework, but rather use the test statistic as a metric of relative sample quality. We also compute the following quantities on the real and generated samples: a) temporal correlation coefficient, b) channel-wise correlation coefficient, and c) the frequency spectrum for each channel averaged over samples. For each of these three features, we use the sum of absolute difference between features computed from real and synthesized data as a metric of similarity. A small number means the generated data is close to real data based on the corresponding feature.

As the results in Figure 8 show, the different metrics do not agree in general. Nonetheless, COT-GANs in general outperform other models. According to MMD and temporal correlation, direct minimization of the mixed Sinkhorn divergence is as good as the best COT-GAN with $\lambda = 1.0$. But all COT-GANs do better in channel correlation and frequency spectrum. We noticed that increasing λ is helpful for MMD and the two correlations, but is not for frequency spectrum.

Model and training parameters. The dimensionality of the latent state is 10 at each time step, and there is also a 10-dimensional time-invariant latent state. The generator common to COT-GAN, direct minimization and Sinkhorn GAN comprises a 1-layer (synthetic) or 2-layer (EEG) LSTM networks, whose output at each time step is passed through two layers of fully connected ReLU networks. We used Adam for updating θ and φ , with learning rate 0.001. Batch size is 32 for all methods except for direct minimization of the original Sinkhorn divergence which is trained with batch size 64. These hyperparameters do not substantially affect the results.

The same discriminator architecture is used for both h and M in COT-GAN and the discriminator of the Sinkhorn GAN. This network has two layers of 1-D causal CNN with stride 1, filter length 5. Each layer has 32 (synthetic data) or 64 neurons (EEG) at each time step. The activation is ReLU except at the output which is linear for autoregressive process, sigmoid for noisy oscillation, and tanh for EEG. For COT-GAN, $\lambda = 10.0$ and $\epsilon = 10$ for synthetic datasets, and $\lambda \in \{0.01, 0.1, 1.0\}$ and $\epsilon = 100.0$ for EEG. The choice of ϵ is made based on how fast it converges to a particular threshold of the transport plan, and each iteration takes around 1 second on a 2.6GHz Xeon CPU.

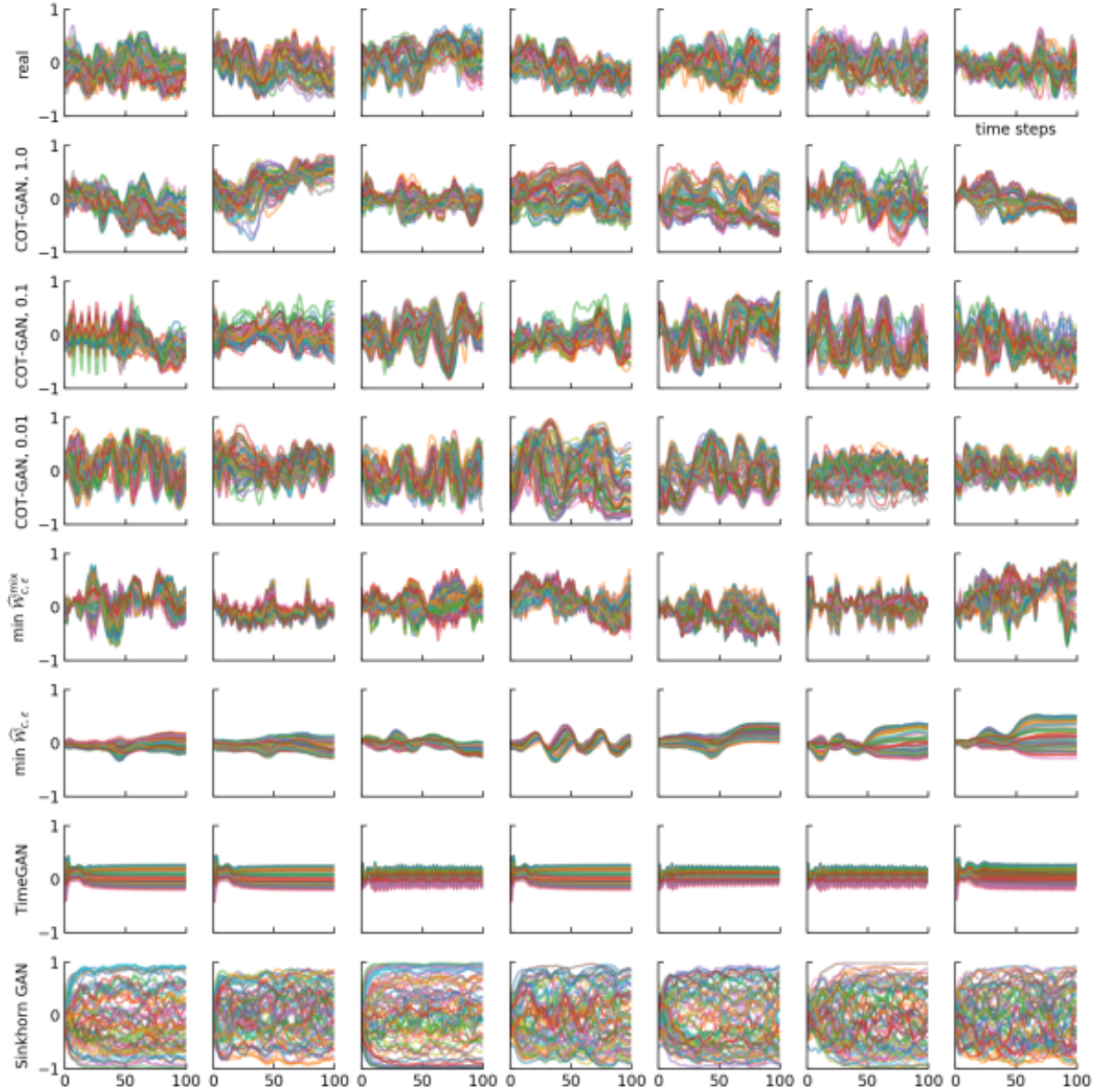


Figure 7: Data and samples obtained by different methods for EEG data, the number after COT-GAN indicates the value of λ .

B.2 Videos datasets

B.2.1 Sprite animations

Data pre-processing. The sprite sheets can be created and downloaded from ³. The data can be generated with various feature options for clothing, hairstyle and skin color, etc. Combining all feature options gives us 6352 characters in total. Each character performs spellcast, walk, slash, shoot and hurt movements from different directions, making up to a total number of 21 actions. As the number of frames T ranges from 6 to 13, we pad all actions to have the same length $T = 13$ by repeating previous movements in shorter sequences. We then crop the characters from sheets to be in the center of each frame, which gives a dimension of $64 \times 64 \times 4$ for each frame. We decide to drop the 4th channel

³gaurav.munjal.us/Universal-LPC-Spritesheet-Character-Generator/
and github.com/jrconway3/Universal-LPC-spritesheet

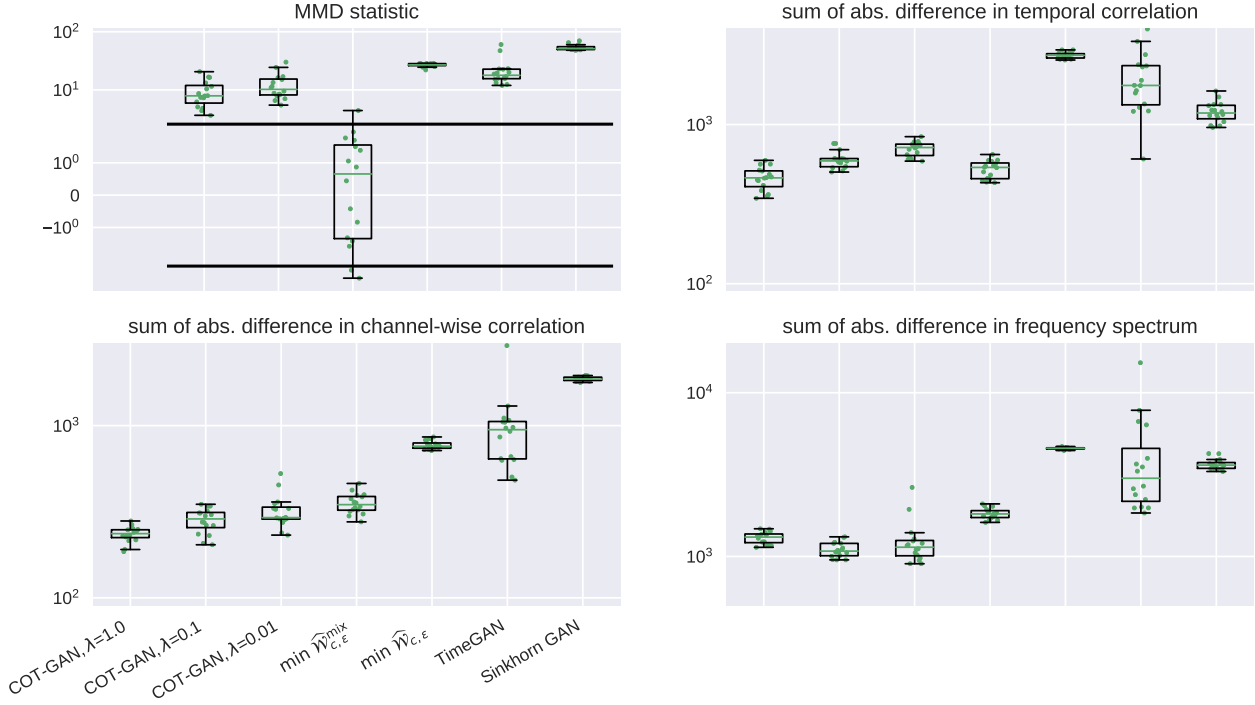


Figure 8: EEG data evaluations. Top left, MMD statistic. More positive means COT-GAN $\lambda = 1.0$ is better, and more negative means COT-GAN $\lambda = 1.0$ is worse. The two horizontal lines indicate statistical significance thresholds ($\alpha = 0.01$, two-tailed). For the other panels, lower value means the feature of generated data is closer to the feature of real data.

Table 2: Generator architecture.

Generator	Configuration
Input	$z \sim \mathcal{N}(\mathbf{0}, \mathbf{I})$
0	LSTM(state size = 128), BN
1	LSTM(state size = 256), BN
2	Dense(8*8*512), BN, LeakyReLU
3	reshape to 4D array of shape (m, 8, 8, 512) as input for DCONV
4	DCONV(N512, K5, S1, P=SAME), BN, LeakyReLU
5	DCONV(N256, K5, S2, P=SAME), BN, LeakyReLU
6	DCONV(N128, K5, S2, P=SAME), BN, LeakyReLU
7	DCONV(N3, K5, S2, P=SAME)

(alpha channel) to be consistent with the input setting of baseline models. Finally, the resulting dataset has 6352 data points consisting of sequences with 13 frames of dimension $64 \times 64 \times 3$.⁴

B.2.2 The Weizmann Action database

Data pre-processing. The videos in this dataset consists of clips that have lengths from 2 to 7 seconds. Each second of the original videos contains 25 frames, each of which has dimension 144x180x3. To avoid the absence of objects at the beginning of the videos and to ensure having an entire evolution of motions in each sequence, we skip the first 5 frames, then skip every 2 frames and collect 16 frames in a whole sequence as a result. Due to limited access to hardware, we also downscale each frame to $64 \times 64 \times 3$. The training set used contains 89 data points with dimension $16 \times 64 \times 64 \times 3$.

⁴To facilitate the use of large dataset in TensorFlow, we pre-shuffled all data used and wrote into tfrecord files. Links for download can be found on the Github repository.

Table 3: Discriminator architecture.

Discriminator	Configuration
Input	64x64x3
0	CONV(N128, K5, S2, P=SAME), BN, LeakyReLU
1	CONV(N256, K5, S2, P=SAME), BN, LeakyReLU
2	CONV(N512, K5, S2, P=SAME), BN, LeakyReLU
3	reshape to 3D array of shape (m, T, -1) as input for LSTM
4	LSTM(state size = 512), BN
5	LSTM(state size = 128)

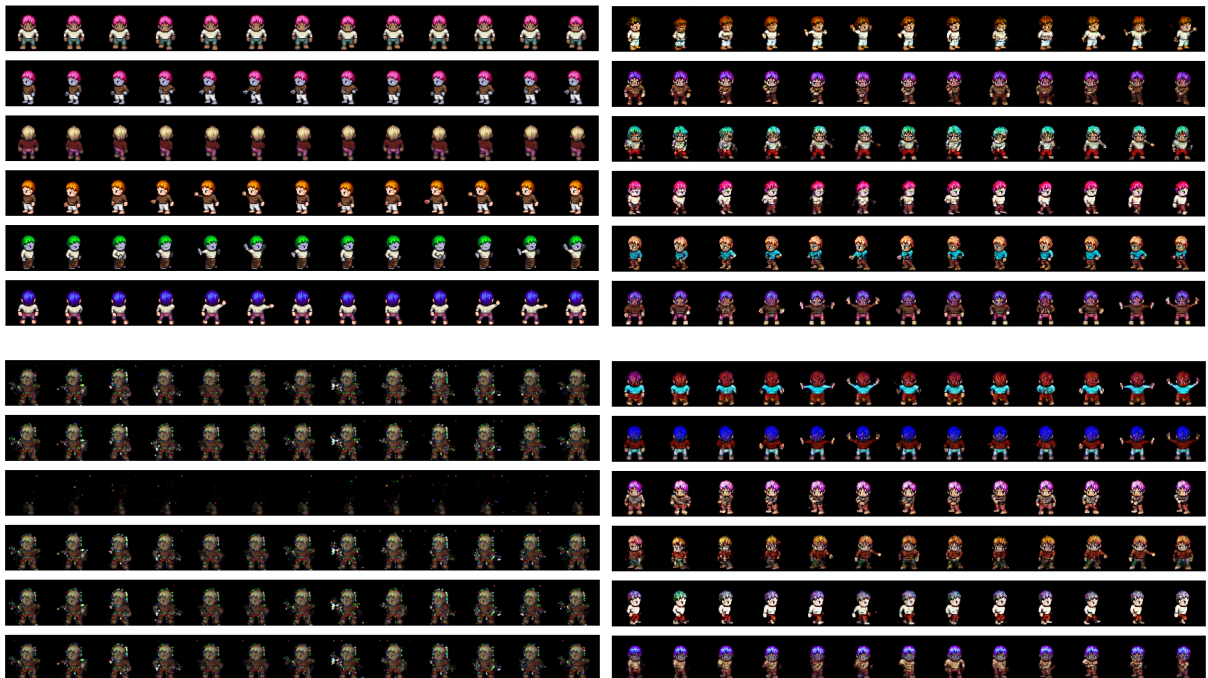


Figure 9: Random samples with no cherry picking from models trained on animated Sprites. Top row from left to right: real sequences and mixed Sinkhorn minimization; bottom row from left to right: MoCoGAN and COT-GAN.

GAN architectures. We detail the GAN architectures used in the experiment of the Weizmann Action database in Table 2 and Table 3. A latent variable z of shape 5×5 per time step is sampled from a multivariate standard normal distribution and is then passed to a 2-layer LSTM to generate time-dependent features, followed by 4-layer deconvolutional neural network (DCONV) to map the features to frames. In order to connect two different types of networks, we map the features using a feedforward (dense) layer and reshape them to the desired shape for DCNN. In Table 2 and 3, the DCONV layers have N filter size, K kernel size, S strides and P padding option. We adopted batch-normalisation layers and the LeakyReLU activation function. We have two networks to parameterize the process h and M as discriminator share the same structure, shown in Table 3.

Note that we did not use random projector in this experiments. Moreover, we used a fixed length $T = 16$ of LSTM and the state size in the last LSTM layer corresponds to the dimension of h_t and M_t , i.e., j in (3.9). We also applied exponential decay to learning rate by $\eta_t = \eta_0 r^{s/c}$ where η_0 is the initial learning rate, r is decay rate, s is the current number of training steps and c is the decaying frequency. In our experiments, we set the initial learning rate to be 0.001, decay rate 0.98, and decaying frequency 500. The batch size m and time steps T used are both 16, $\lambda = 0.01$, $\epsilon = 6.0$ and the Sinkhorn $L = 100$ in this experiment. We trained COT-GAN on a single NVIDIA Tesla P100 GPU. Each iteration takes roughly 1.5 seconds.

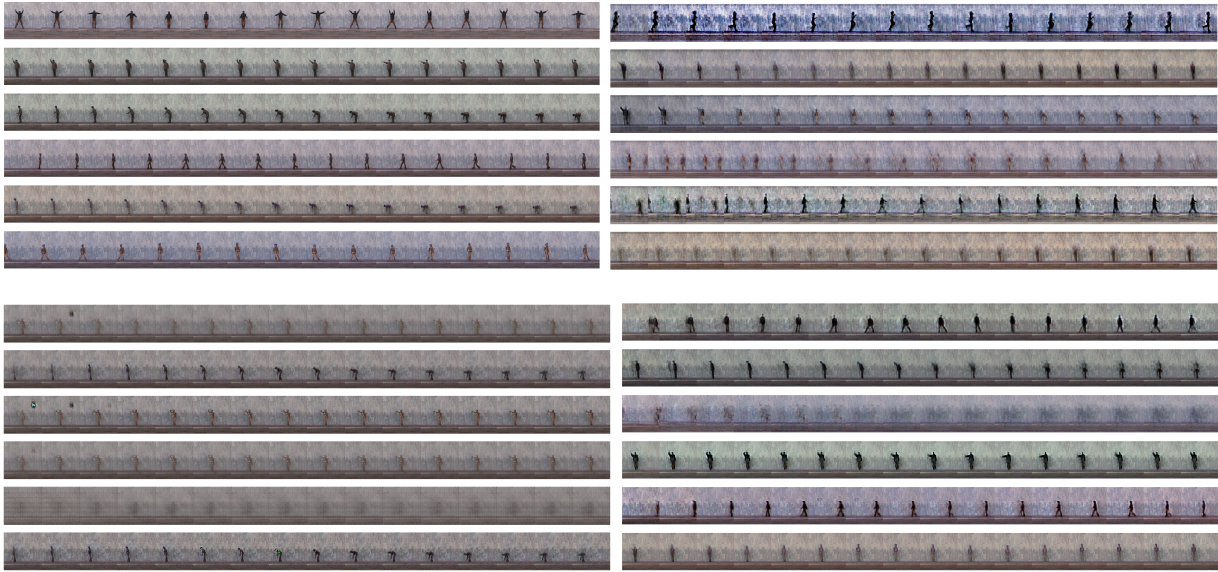


Figure 10: Random samples with no cherry picking from models trained on human actions. Top row from left to right: real sequences and mixed Sinkhorn minimization; bottom row from left to right: MoCoGAN and COT-GAN.

C Sprites and human action results without cherry-picking

In this section we show random samples of Sprites and human actions generated by COT-GAN, mixed Sinkhorn minimization, and MoCoGAN without cherry-picking. The background was static for both experiments. In the Sprites experiments (see Figure 9), the samples from mixed Sinkhorn minimization and COT-GAN are both of good quality, whereas those from MoCoGAN only capture a rough pattern in the frames and fail to show a smooth evolution of motions.

In Figure 10, we show a comparison of real and generated samples for human action sequences. Noticeable artifacts of COT-GAN and mixed Sinkhorn minimization results include blurriness and even disappearance of the person in a sequence, which normally happens when the clothing of the person has a similar color as the background. MoCoGAN also suffers from this issue and, visually, there appears to be some degree of mode collapse. We used generators of similar capacity across all models and trained COT-GAN, mixed Sinkhorn minimization and MoCoGAN for 65000 iterations.

In Table 4 the evaluation scores are estimated using 10000 generated samples. We increased the sample size from 5000 samples for Table 1 to 10000 samples in order to yield more robust evaluation metrics. For Sprites, COT-GAN performs better than the other two methods on FVD and KVD. However, minimization of the mixed Sinkhorn divergence produces slightly better FID and KID scores when compared to COT-GAN. The results in [37] suggest that FID better captures the frame-level quality, while FVD is better suited for the temporal coherence in videos. For the human action dataset, COT-GAN is the best performing method across all metrics except for KVD. It is also reported in [37] that, while FVD and KVD are highly correlated, the former agrees with human judgement better than the latter.

Table 4: Evaluations for video datasets. Lower value indicates better sample quality.

Sprites	FVD	FID	KVD	KID
MoCoGAN	1108.2	280.25	146.8	0.34
$\min \widehat{\mathcal{W}}_{c,\varepsilon}^{\text{mix}}$	498.8	81.56	83.2	0.078
COT-GAN	458.0	84.6	66.1	0.081
Human actions				
MoCoGAN	1034.3	151.3	89.0	0.26
$\min \widehat{\mathcal{W}}_{c,\varepsilon}^{\text{mix}}$	507.6	120.7	34.3	0.23
COT-GAN	462.8	58.9	43.7	0.13